Materials
Horizons

COMMUNICATION

View Article Online
View Journal

Cite this: DOI: 10.1039/d4mh01582g

Received 5th November 2024,
Accepted 2nd April 2025

DOI: 10.1039/d4mh01582g

rsc.li/materials-horizons

Modeling and design of 3D printed hyperelastic lattice metamaterials with bionic S-shaped stress–strain behaviors†

Le Dong,[ab] Mengjie Zhang[ab] and Dong Wang *[ab]

Lattice metamaterials made of stiff polymers, ceramics, and metals have been extensively designed to reproduce the mechanical behaviors of biological tissues, holding promising applications in biomedical devices and tissue engineering. However, lattice metamaterials composed of soft materials have been far less explored due to challenges posed by material nonlinearity and large deformations. Here, hyperelastic lattice metamaterials with curved microstructures are fabricated by 3D printing elastomers and are developed to mimic bionic S-shaped stress–strain behaviors. We propose a design framework for 3D printed hyperelastic lattice metamaterials that integrates digital geometry generation, hierarchical mechanics modeling, and validation by finite element (FE) simulations and experiments. The microstructures are modeled through deriving a Timoshenko-type beam theory governed by hyperelastic strain energy potentials. The model is then combined with the deformation and equilibrium analysis considering non-rigid connections between microstructures to predict the mechanical responses of hyperelastic lattice metamaterials. Using the developed design framework, programmable S-shaped stress–strain behaviors and high fracture strains (over 800%) are achieved. We demonstrate S-shaped stress–strain curves that match skeletal and cardiac muscles and highly stretchable lattice sensors for remote controls. This study provides design methods and theoretical guidelines for hyperelastic lattice metamaterials, holding promise for robotic sensors with bionic performance and functionality.

New concepts

This work introduces the concept of hyperelastic lattice metamaterials for bionic S-shaped stress–strain behaviors. Unlike traditional lattice metamaterials composed of stiff materials, hyperelastic lattice metamaterials are made of elastomers and feature curved microstructures. They can mimic the hyperelastic characteristics of biological materials and exhibit bionic S-shaped stress–strain curves. 3D printing technology is utilized to achieve precise and rapid fabrication. We propose a design framework for 3D printed hyperelastic lattice metamaterials that integrates geometry generation, mechanics modeling, and both experimental and simulated validation. Guided by the framework, the S-shaped stress–strain behaviors can be programmed by tuning the design parameters. We demonstrate the S-shaped stress–strain behaviors that match skeletal and cardiac muscles, as well as highly stretchable lattice sensors for robotic remote controls. This framework can accurately predict the local large deformations and the effects of non-periodic boundary conditions, offering quantitative guidance for robot sensor design and biomedical applications.

1. Introduction

Artificial materials with biomimetic mechanical behaviors hold great promise for biomedical devices,[1–3] tissue engineering,[4–6] and soft robots.[7–9] Biology provides extensive guidance for building such materials through structured design.[10,11] Many biological tissues, such as skin,[12] tendons,[13] blood vessels[14] and cardiac tissue,[15] exhibit two-stage stress–strain responses under uniaxial stretching owing to their inner curved and intertwined microstructures (*e.g.*, elastin and collagen fibers in Fig. 1a). Initially, elastin and collagen fibers unfurl and align with the loading direction, resulting in negligible stiffness, shown as the toe region (stage I). As the applied strain increases, the fibers straighten, and their stretching dominates the mechanical response, leading to a sharp increase in the tangent modulus (stage II). For elastin-rich tissues (*e.g.*, skin and iliac artery), stage II is linear because elastin is highly linear elastic, forming a J-shaped stress–strain curve (Fig. 1b). Conversely, for collagen-rich tissues (*e.g.*, skeletal and cardiac muscles), stage II is nonlinear due to the hyperelastic nature of collagen, resulting in an S-shaped stress–strain curve (Fig. 1c). For instance, uniaxial tensile tests have revealed the hyperelastic behavior of collagen with a 90% fracture strain[16,17] and the S-shaped stress–strain curves of skeletal muscles with over 400% fracture strain.[18] These two-stage stress–strain behaviors

---

[a] *State Key Laboratory of Mechanical System and Vibration, School of Mechanical Engineering, Shanghai Jiao Tong University, Shanghai 200240, China. E-mail: wang_dong@sjtu.edu.cn*

[b] *Shanghai Key Laboratory of Intelligent Robotics, Meta Robotics Institute, Shanghai Jiao Tong University, Shanghai 200240, China*

† Electronic supplementary information (ESI) available. See DOI: **https://doi.org/10.1039/d4mh01582g**

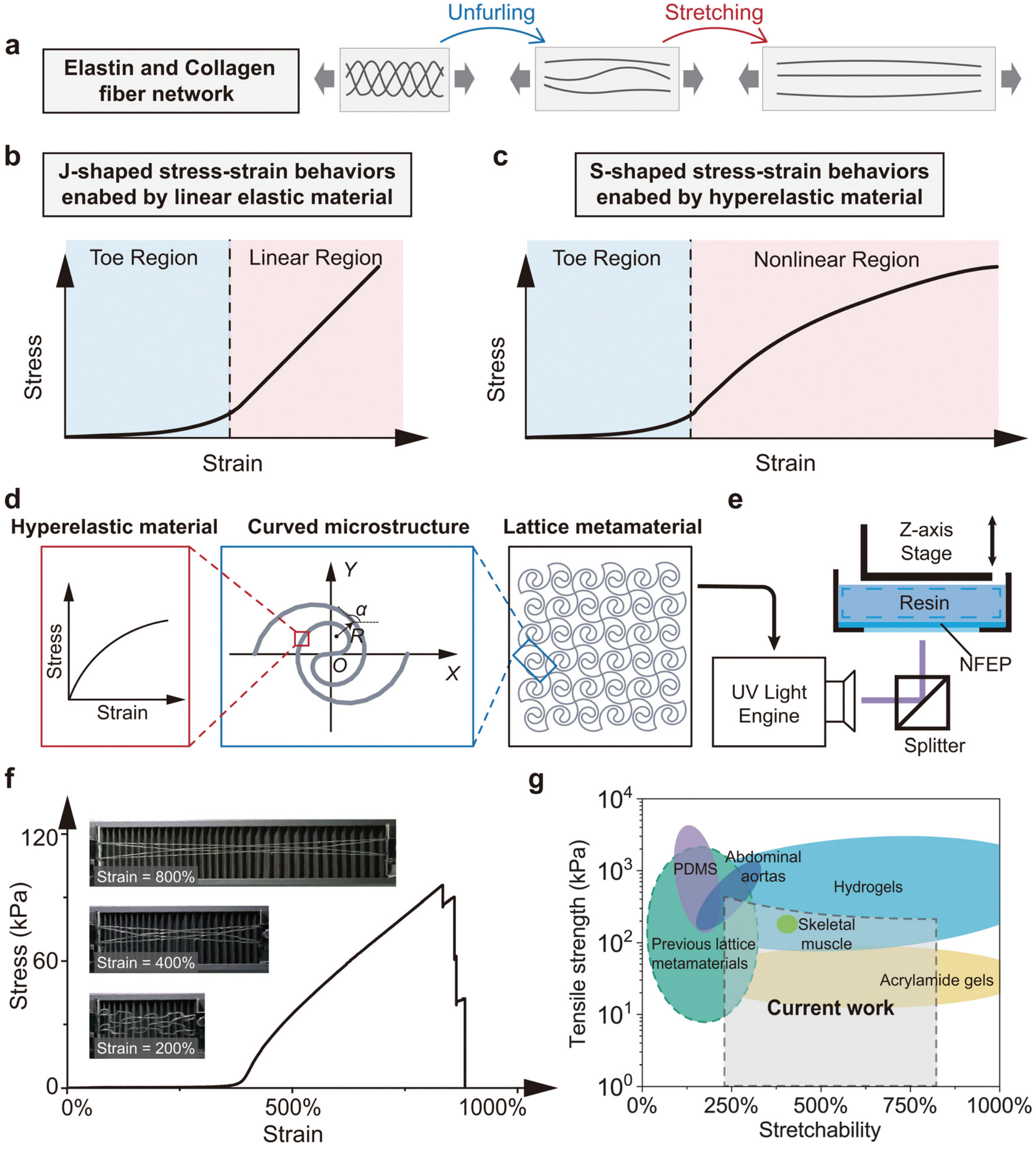

Fig. 1 Design concept of hyperelastic lattice metamaterials. (a) Two-stage deformation of elastin and collagen fiber network in biological tissue under uniaxial stretching. (b) Linear elastic material enabled J-shaped stress–strain curve showing toe and linear regions. (c) Hyperelastic material enabled S-shaped stress–strain curve showing toe and nonlinear regions. (d) Geometry of hyperelastic lattice metamaterials, consisting of three hierarchical structures: microstructures, lattice units, and lattice metamaterials. (e) Custom DLP printing system. (f) High stretchability of the designed hyperelastic lattice metamaterial. (g) Ashby plot of tensile strength *versus* stretchability for various soft materials, biological tissues, previously studied 3D printed lattice metamaterials, and the proposed hyperelastic lattice metamaterials.

can provide natural mechanisms to protect biological tissues from excessive strain.[19]

With the rapid advancement of 3D printing,[20–22] lattice metamaterials have been developed with a bioinspired microstructure made of stiff polymers, metals, and ceramics.[23–25] They can reproduce the J-shaped stress–strain behaviors of biological tissues, showing extensive applications in flexible network scaffolds,[26] electronic skin,[27] and wearable exoskeletons.[28] Examples include triangular lattice metamaterials with horseshoe microstructures replicating the mechanics of human skin,[29] rectangular lattice metamaterials with wavy microstructures exhibiting mechanical properties similar to the iliac artery,[30] and cylindrical lattice metamaterials with serpentine microstructures displaying nerve tissue-like mechanical responses.[31] Compared with these existing lattice metamaterials made of stiff constituents, the hyperelastic lattice metamaterials made of elastomers can feature S-shaped stress–strain curves and higher stretchability. However, the development of hyperelastic lattice metamaterials is hindered by the lack of theoretical models and design methods.

Many theoretical models have been developed for lattice metamaterials with J-shaped stress–strain behaviors to effectively guide structural design.[32] So far, both phenomenological and micromechanics models have been established. For example, Cao *et al.* proposed a single-parameter phenomenological framework, incorporating a two-segment model to capture the J-shaped stress–strain relationship.[33] While the expressions are simple and explicit, they sacrifice a certain degree of prediction accuracy and overlook the nonlinearity in the stretching-dominated deformation stage. A pioneering micromechanics model by Ma *et al.* combines the curved Kirchhoff-type beam theory of the microstructures with equilibrium equations and deformation compatibility of the lattices to predict the mechanical behaviors of lattice metamaterials.[34] This hierarchical model is later extended to lattice metamaterials with fractal microstructures,[35] rotatable nodes,[36] and multi-materials.[37] Notably, most of these micromechanics models are based on the key assumption of the linear elastic material, which holds for small local strain (below 5%). As a result, they can be used for lattice metamaterials with J-shaped stress–strain curves under moderate deformation (below 100%), but not for hyperelastic lattice metamaterials under large deformation (above 400%), where finite local strains arise. Recently, a few theoretical models for hyperelastic lattice metamaterials with straight microstructures have been reported.[38] These models use the principle of stationary potential energy to calculate stress–strain behavior based on affine deformation assumptions. Although the energy-based methods are mathematically concise, they are not valid for curved microstructures which undergo non-affine deformation under large stretching. Therefore, finite deformation models for hyperelastic lattice metamaterials that simultaneously consider curved microstructures and material hyperelasticity are needed.

In this work, we develop a design framework for 3D printed hyperelastic lattice metamaterials constructed from curved microstructures, integrating digital geometric generation, finite deformation theoretical modeling, and validation through FE simulations and experiments. The curved microstructures are modeled as Timoshenko-type beams governed by various strain energy density functions to account for material hyperelasticity. The overall mechanical response is derived using a discretization formulation within a variational framework. By combining the mechanics analysis of microstructures with the analysis of deformation compatibility and equilibrium, we study the mechanical responses of hyperelastic lattice metamaterials under periodic and non-periodic boundary conditions. The non-rigid connections between microstructures induced by finite deformations, *i.e.*, variable angles between the tangent lines of different microstructures, are considered. The designed hyperelastic lattice metamaterials can achieve programmable S-shaped stress–strain curves and high stretchability (over 800% shown in Fig. 1f). Fig. 1g displays an Ashby plot of tensile strength *versus* stretchability for the hyperelastic lattice metamaterial in this work, existing lattice metamaterials,[29,39–45] various biological tissues[18,46] and typical soft materials.[47–49] The Ashby plot indicates that the developed hyperelastic lattice metamaterials offer greater stretchability (up to 850%) and relatively lower tensile strength (below 440 kPa) compared to existing 3D printed lattice metamaterials, making them well-suited for mimicking soft biological tissues with large deformations. This work focuses on the understanding and design of S-shaped stress–strain behaviors using hyperelastic lattice metamaterials. S-shaped stress–strain behaviors that mimic biological tissues have been designed. The highly stretchable lattice sensors with predictable electrical properties and remote control capability are showcased. To the best of our knowledge, such a framework has not been explored before.

2. Structural geometry and 3D printing fabrication

2.1. Geometry and digital design

Fig. 1d depicts the design concept and representative geometries of hyperelastic lattice metamaterials. The metamaterials are made of hyperelastic elastomers and exhibit a hierarchical configuration consisting of microstructures, lattice units, and lattice metamaterials. The design process involves three steps: First, hyperelastic materials are used to form anti-symmetrical microstructures, with geometries based on curvature functions $R(\alpha)$ that define the relationship between the slope angle α and the instantaneous radius of curvature R. Second, the lattice units are generated by connecting curved microstructure following the rectangular pattern. Lastly, the hyperelastic lattice metamaterials are constructed by periodically arranging the lattice units. An automatic digital design workflow is developed in the algorithmic design environment Rhino Grasshopper to perform the above design steps and obtain the manufacturing representations (STL files). Due to the hierarchical geometric construction, mechanics analysis is conducted at two different levels: the hyperelastic microstructure and the hyperelastic lattice metamaterial, as detailed in Sections 3 and 4, respectively.

2.2. Material characterization and 3D printing process

The designed hyperelastic lattice metamaterials are fabricated using digital light processing (DLP) 3D printing. The home-made DLP printing system is composed of a UV-projector (DLi 3DLP9000), a beam splitter, a resin tank with a transparent glass window coated with transparent fluorinated polymer (NFEP) film, and a linear translation stage (Fig. 1e). The resolution of the UV projector used is 2560 pixels × 1600 pixels. Each pixel has a size of 42 μm × 42 μm. The layer thickness is set to 50 μm. A commercial UV-curable resin (65A, QIEFENG Co, China) is employed for manufacturing (Section S4 and S5, ESI†). Tensile tests are conducted to obtain the material nominal stress–strain behaviors using a uniaxial material testing system (Instron 68SC-2) with a tensile rate of 2 mm min^{-1} (Section S6, ESI†). The material exhibits a stretchability of ∼160%. The hyperelastic properties are measured by fitting with the Neo-Hookean model using MatEditor (WELSIM), yielding the fitted material constant c_1 = 0.733 MPa for the strain energy density function $W = c_1(I_C - 3)$, where I_C

denotes the first invariant of the right Cauchy–Green tensor (Fig. S1a, ESI†).

3. Theoretical model of hyperelastic curved microstructures

In this section, the mechanics of hyperelastic microstructures are investigated within a discretized framework by extending the two-dimensional geometrically exact beam theory to incorporate various hyperelastic constitutive equations.[50,51] The deformation of the microstructures accounting for axial, shear, and bending strains under applied forces and moments is obtained numerically.

3.1. Kinematics of deformation

When the lattice metamaterials undergo large uniaxial stretching, each microstructure experiences non-affine deformation due to the nonlinear material and curved geometry, resulting in the complexity of developing an analytical model *via* energy methods and static equilibrium equations. Thus, the hyperelastic beam formulations within the discretization framework are derived to model the microstructures. As shown in Fig. 2b, each half of the undeformed microstructure is discretized into n_e straight beam elements. The coordinates of the start point

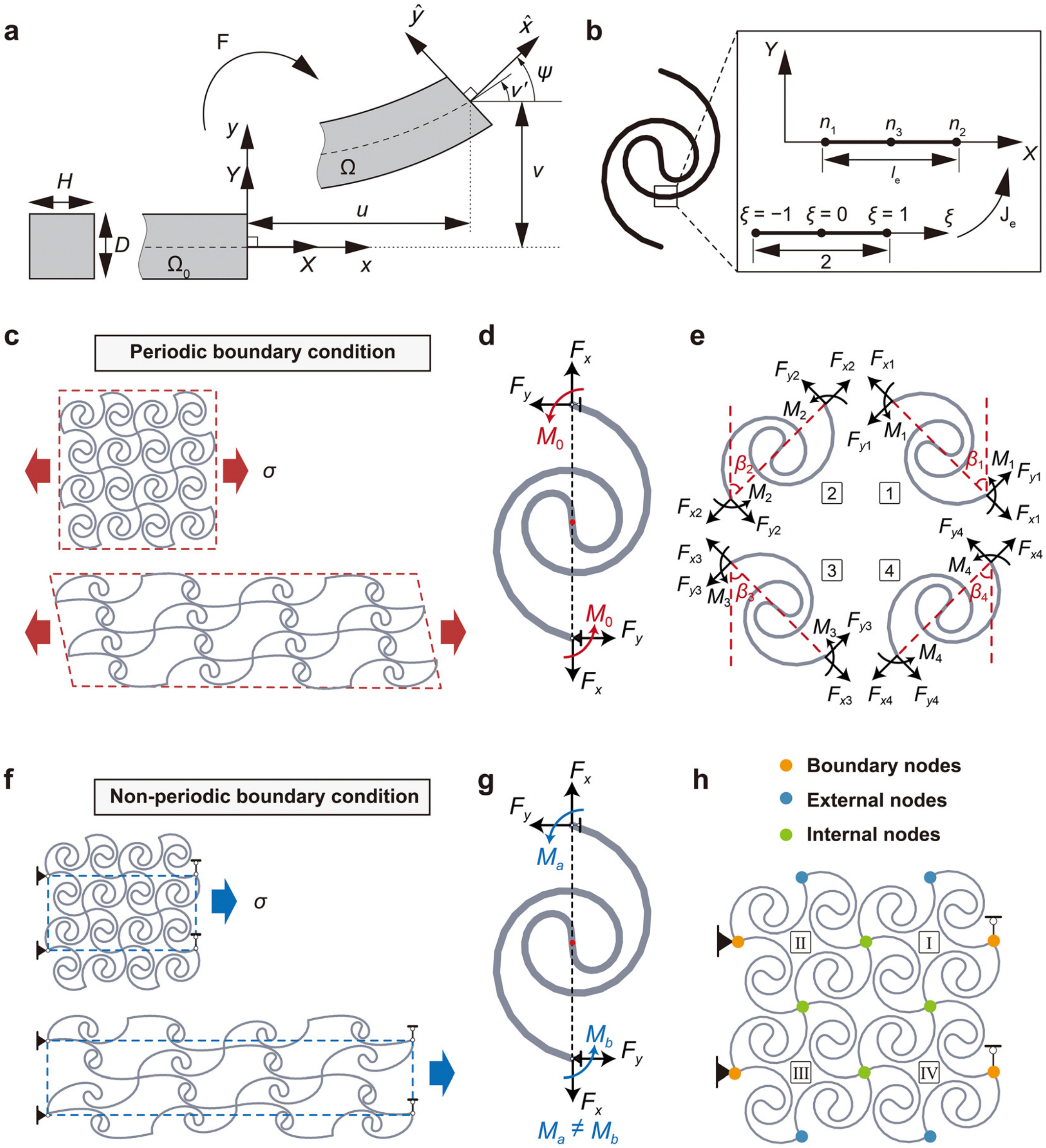

Fig. 2 Theoretical model for hyperelastic lattice metamaterials. (a) Nonlinear kinematics of Timoshenko-type beams. (b) Quadratic elements in the Timoshenko beam-type nonlinear formulation for hyperelastic microstructures. (c) Hyperelastic lattice metamaterials with periodic boundary conditions. (d) Schematic of a microstructure under axial force F_x, shear force F_y, and moment M_0 at two ends. (e) Inner forces and moments for each microstructure in the representative units. (f) Hyperelastic lattice metamaterials with non-periodic boundary conditions. (g) Schematic of a microstructure under an axial force F_x, shear force F_y, and moment M_a and M_b at two ends. (h) Categorization of connected nodes: boundary nodes, external nodes, and internal node.

($X_{\mathrm{S}i}$, $Y_{\mathrm{S}i}$) and end point ($X_{\mathrm{E}i}$, $Y_{\mathrm{E}i}$) of the ith element are given by

$$\begin{cases} \begin{pmatrix} X_{\mathrm{S}i} \\ Y_{\mathrm{S}i} \end{pmatrix} = \displaystyle\int_0^{\alpha_{i-1}} R(\alpha) \begin{pmatrix} \cos\alpha \\ \sin\alpha \end{pmatrix} \mathrm{d}\alpha, \\ \begin{pmatrix} X_{\mathrm{E}i} \\ Y_{\mathrm{E}i} \end{pmatrix} = \displaystyle\int_0^{\alpha_{i}} R(\alpha) \begin{pmatrix} \cos\alpha \\ \sin\alpha \end{pmatrix} \mathrm{d}\alpha \end{cases} \quad \text{for } i = 1, \ldots, n_{\mathrm{e}}, \tag{1}$$

where $\alpha_i = i\alpha_{\mathrm{end}}/n_{\mathrm{e}}$. The α_{end} is determined by solving $Y(\alpha) = \int_0^{\alpha_{\mathrm{end}}} R(\alpha)\sin\alpha \mathrm{d}\alpha = 0$.

Consider a beam element with length l_{e} and rectangular cross-section with width D and height H as illustrated in Fig. 2a. The stress-free reference and current configurations are denoted by Ω_0 and Ω, respectively. To describe the kinematics of beam deformation, a global Cartesian coordinate system X, Y and an orthonormal local coordinate x, y are used. The two coordinate systems are coincident for reference configurations and located at the geometric center of the beam. x is identified as the tangent vector of the centerline and y lies along the width directions. $\{\hat{x}, \hat{y}\}$ is the local coordinate in the current configuration.

Given a centerline displacement vector $\mathbf{u} = \{u,v,\psi\}$, where u is the displacement in the axial direction, v is the deflection and ψ is the rotation, the displacement vector $\mathbf{U}$ of a material point of the beam from initial position $\mathbf{X}$ (X, Y) to deformed position $\boldsymbol{x}$ (x, y) can be described by $\mathbf{u}$ as follows:

$$\mathbf{U}(\mathbf{X}) = \begin{Bmatrix} X + u(X) \\ v(X) \\ \psi \end{Bmatrix} + Y \begin{Bmatrix} -\sin\psi(X) \\ \cos\psi(X) \\ 0 \end{Bmatrix}. \tag{2}$$

The relation between the strain vector $\boldsymbol{\varepsilon}$ and the displacement vector $\mathbf{u}$ is derived from the principle of virtual work,[52] given by

$$\boldsymbol{\varepsilon} = \mathbf{T}(\psi)\mathbf{u}' - \mathbf{N} \tag{3}$$

where $\boldsymbol{\varepsilon} = \begin{Bmatrix} \varepsilon \\ \gamma \\ \kappa \end{Bmatrix}$, $\mathbf{T}(\psi) = \begin{bmatrix} \cos\psi & \sin\psi & 0 \\ -\sin\psi & \cos\psi & 0 \\ 0 & 0 & 1 \end{bmatrix}$, $\mathbf{u}' = \begin{Bmatrix} 1 + u' \\ v' \\ \psi' \end{Bmatrix}$ and $\mathbf{N} = \begin{Bmatrix} 1 \\ 0 \\ 0 \end{Bmatrix}$. ε is the axial strain, γ is the shear strain and κ is the curvature. $()'$ denotes the derivative with respect to the coordinate X.

3.2. Constitutive equations

Consider a beam constructed using an incompressible hyperelastic material. The stress–strain constitutive relationship is defined from a strain energy density function W that depends on the deformation gradient $\mathbf{F}$. For a Timoshenko beam in the x–y plane, the deformation gradient is defined as

$$\mathbf{F} = \begin{bmatrix} \lambda_x & 0 & 0 \\ \gamma & \lambda_y & 0 \\ 0 & 0 & \lambda_z \end{bmatrix}, \tag{4}$$

where λ_x, λ_y and λ_z are the stretches in axial, width and height directions, respectively. Note that the axial stretching satisfies $\lambda_x = \varepsilon + \kappa y + 1$. On the centerline ($y = 0$), the axial stretch $\lambda_c = \varepsilon + 1$. The Cauchy stress tensor σ is obtained by

$$\boldsymbol{\sigma} = \frac{\partial W}{\partial \mathbf{F}}\mathbf{F}^{\mathrm{T}} - p\mathbf{I}, \tag{5}$$

where p denotes the Lagrange multiplier to ensure incompressibility and $\mathbf{I}$ is the identity matrix. By solving the plane stress assumptions $\sigma_{yy} = 0$ and $\sigma_{zz} = 0$ in the transverse plane, along with the incompressibility constraint $\det(\mathbf{F}) = 1$, the stretches λ_y, λ_z and the p can be calculated. Accordingly, the stress resultant vector $\mathbf{S}_{\mathrm{r}}$ in the current configuration is given by

$$\mathbf{S}_{\mathrm{r}} = \begin{cases} N = \displaystyle\int_{-d/2}^{d/2} \sigma_{xx}(\hat{y}) b \mathrm{d}\hat{y} \\ Q = \displaystyle\int_{-d/2}^{d/2} \sigma_{xy}(\hat{y}) b \mathrm{d}\hat{y} \quad , \\ M = \displaystyle\int_{-d/2}^{d/2} \sigma_{xx}(\hat{y}) \hat{y} b \mathrm{d}\hat{y} \end{cases} \tag{6}$$

where N is the axial resultant force in the $\hat{x}$ direction, Q donates the resultant shear force in the $\hat{y}$ direction, and M is the resultant moment acting on the beam cross-section. To describe the cross-section variation due to stretching, the width and height are updated by $d = \int_{-D/2}^{D/2} \lambda_y(Y)\mathrm{d}Y$ and $h = \frac{H}{D}\int_{-D/2}^{D/2} \lambda_z(Y)\mathrm{d}Y$. Deriving the resultant stress with respect to the strain variables produces the stiffness matrix $\mathbf{D}$ as

$$\mathbf{D} = \frac{\partial \mathbf{S}_{\mathrm{r}}}{\partial \boldsymbol{\varepsilon}}. \tag{7}$$

For the incompressible Neo-Hookean material, the Cauchy stress tensor derived from the strain energy density function is given by

$$\boldsymbol{\sigma} = 2c_1\mathbf{F}\mathbf{F}^T - p\mathbf{I}. \tag{8}$$

Considering the deformation gradient $\mathbf{F}$ shown in eqn (4), the normal and tangential Cauchy stress components acting on the beam cross-section are calculated as

$$\sigma_{xx} = -\frac{c_1\left(\gamma^2(\lambda_{\mathrm{c}} + \kappa y) + \sqrt{4 + \gamma^4(\lambda_{\mathrm{c}} + \kappa y)^2} - 2(\lambda_{\mathrm{c}} + \kappa y)^3\right)}{\lambda_{\mathrm{c}} + \kappa y}, \tag{9}$$

$$\sigma_{xy} = 2c_1\gamma(\lambda_{\mathrm{c}} + \kappa y). \tag{10}$$

Similarly, for the incompressible Mooney–Rivlin material, eqn (8) becomes

$$\begin{cases} W = c_1(I_C - 3) + c_2(II_C - 3), \\ \sigma = 2c_1\mathbf{F}\mathbf{F}^{\mathrm{T}} - 2c_2\left(\mathbf{F}\mathbf{F}^{\mathrm{T}}\right)^{-1} - p\mathbf{I}. \end{cases} \tag{11}$$

where II_C is the second invariant of the right Cauchy–Green tensor and c_i (i = 1 and 2) are material constants. The corresponding normal and tangential Cauchy stress components can be obtained by

$$\begin{aligned} \sigma_{xx} =\ & 2c_1(\lambda_c + \kappa y)^2 \\ & - \frac{c_1\left(\sigma_1 + 2c_2^2(\lambda_c + \kappa y)^3 + c_1\gamma^2(\lambda_c + \kappa y)\right)}{c_2(\lambda_c + \kappa y)^3 + c_1(\lambda_c + \kappa y)} \\ & - \frac{2c_2\left(\sigma_1 + 2c_2^2(\lambda_c + \kappa y)^3 + c_1\gamma^2(\lambda_c + \kappa y)\right)}{(\lambda_c + \kappa y)^2(\sigma_1 - c_1\gamma^2(\lambda_c + \kappa y))} \\ & + \frac{4c_2(\lambda_c + \kappa y)\left(c_2(\lambda_c + \kappa y)^2 + c_1\right)}{\sigma_1 - c_1\gamma^2(\lambda_c + \kappa y)}, \end{aligned} \tag{12}$$

$$\sigma_{xy} = 2c_1\gamma(\lambda_c + \kappa y) + \frac{4c_2\gamma\left(c_2(\lambda_c + \kappa y)^2 + c_1\right)}{\sqrt{\sigma_1^2 - c_1\gamma^2(\lambda_c + \kappa y)}}, \tag{13}$$

where

$$\sigma_1 = \sqrt{c_1^2\gamma^4(\lambda_c + \kappa y)^2 + 4c_1^2 + 8c_1c_2(\lambda_c + \kappa y)^2 + 4c_2^2(\lambda_c + \kappa y)^4}.$$

By substituting eqn (9), (10) and (12), (13) into eqn (6), the stress resultant vector $\mathbf{S}_\mathbf{r}$ can be numerically calculated. The constitutive matrix **D** is obtained by solving eqn (7) using central finite differences.

3.3. Discretization formulation

The discretization formulation is developed in a variational framework. The microstructure in the reference configuration is discretized into n_e quadratic elements. Each element includes three nodes with degrees of freedom u, v, and ψ (Fig. 2b). Thus, the field variables $\{u,v,\psi\}$ are interpolated by quadratic shape functions as

$$\mathbf{u}_e = \begin{Bmatrix} u_e \\ w_e \\ \psi_e \end{Bmatrix} = \sum_{I=1}^{3} N_I(X) \begin{Bmatrix} u_I \\ w_I \\ \psi_I \end{Bmatrix}, \tag{14}$$

where $N_1(\xi) = \frac{1}{2}(\xi - 1)\xi$, $N_2(\xi) = 1 - \xi^2$ and $N_3(\xi) = \frac{1}{2}(\xi + 1)\xi$ ($\xi \in [-1,1]$). Substituting eqn (14) into eqn (3) yields the explicit form of the strains based on the node displacement vector $\mathbf{u}_I = \{u_I, v_I, \psi_I\}$ as follows:

$$\boldsymbol{\varepsilon}_e = \sum_{I=1}^{3} \mathbf{T}(\psi_e)\mathbf{B}_{0I}\mathbf{u}_I - \mathbf{N} \text{ with } \mathbf{B}_{0I} = N_I'\mathbf{I}. \tag{15}$$

Note that $N_I' = \partial N_I/\partial X = \partial N_I \big/ \partial\xi[\partial X/\partial\xi]^{-1}$. The weak form of equilibrium which is equivalent to the principle of virtual work can be stated as

$$\delta\Pi = \delta\Pi_{\mathrm{int}} - \delta\Pi_{\mathrm{ext}} = 0, \tag{16}$$

where Π donates total energy, Π_{int} is the virtual strain energy of the element and Π_{ext} is the virtual work of external loads acting on that element. Adopting the virtual generalized displacement vector $\delta\mathbf{u}_I^{\mathrm{T}}$, eqn (16) can be expressed by $\delta\mathbf{u}_I^{\mathrm{T}}(\mathbf{f}^\mathbf{e}_{\mathrm{int}\,I} - \mathbf{f}^\mathbf{e}_{\mathrm{ext}\,I}) = 0$, where $\mathbf{f}^\mathbf{e}_{\mathrm{int}\,I}$ and $\mathbf{f}^\mathbf{e}_{\mathrm{ext}\,I}$ are the internal and external forces, respectively (see ESI†). Since $\delta\mathbf{u}_I^{\mathrm{T}}$ is arbitrary,

$$\mathbf{f}^\mathbf{e}_{\mathrm{int}\,I} - \mathbf{f}^\mathbf{e}_{\mathrm{ext}\,I} = 0, \tag{17}$$

which is a system of nonlinear algebraic equations for the nodal degrees of freedom. Linearization of (17) leads to

$$\mathbf{K}^\mathbf{e}\Delta\mathbf{U} = -\mathbf{R} = \mathbf{f}^\mathbf{e}_{\mathrm{int}} - \mathbf{f}^\mathbf{e}_{\mathrm{ext}}, \tag{18}$$

where $\mathbf{K}^\mathbf{e}$ is the element stiffness matrix (see ESI†). $\Delta\mathbf{U}$ is the increment of the generalized displacement vector, which is calculated by the iterative Newton–Raphson method to obtain the deformation of the microstructures.

4. Theoretical model of hyperelastic lattice metamaterials

In this section, the mechanical analysis of microstructures is integrated with the analysis of equilibrium and deformation compatibility in the lattices to predict the mechanical behavior of hyperelastic lattice metamaterials under external loading. In particular, the effect of non-rigid connections between different microstructures induced by finite local deformation is analyzed.

4.1. Periodic boundary conditions

The mechanics of hyperelastic lattices with periodic boundary conditions are investigated. As illustrated in Fig. 2c, each lattice unit comprises four microstructures labeled 1 to 4. When uniaxial vertical stress σ is applied, each microstructure undergoes antisymmetric deformation with respect to the central point due to the antisymmetric geometry. The microstructure is considered as simply supported (Fig. 2d). A vertical force F_x and a horizontal force F_y are applied at each end of the microstructure, and a pair of moments M_0 are antisymmetrically located at the ends (Fig. 2e). The static equilibrium of the lattice unit gives the relationships between internal forces and external loading in both normal and shear direction, which requires that

$$\begin{cases} F_{x1}\cos\beta_1 - F_{y1}\sin\beta_1 + F_{x2}\cos\beta_2 + F_{x2}\sin\beta_2 = 0, \\ F_{x1}\sin\beta_1 + F_{y1}\cos\beta_1 + F_{y4}\sin\beta_4 - F_{y4}\cos\beta_4 = \sqrt{2}LH\sigma, \\ -F_{x1}\sin\beta_1 - F_{y1}\cos\beta_1 + F_{x2}\sin\beta_2 - F_{y2}\cos\beta_2 = 0, \\ -F_{x3}\sin\beta_3 - F_{y3}\cos\beta_3 + F_{x4}\sin\beta_4 - F_{y4}\cos\beta_4 = 0, \\ -F_{x1}\cos\beta_1 + F_{y1}\sin\beta_1 + F_{x4}\cos\beta_4 + F_{y4}\sin\beta_4 = 0, \\ F_{x2}\cos\beta_2 + F_{y2}\sin\beta_2 - F_{x3}\cos\beta_3 + F_{y3}\sin\beta_3 = 0. \end{cases} \tag{19}$$

The moment equilibrium of an arbitrary joint, which is connected by four microstructures, and anti-symmetry requires that

$$\sum_{i=1}^{4} M_i = -\sum_{i=1}^{4} \left(F_{yi} L_i\right)/2 = 0, \tag{20}$$

where L and L_i are the undeformed and deformed lengths between two ends of the microstructures, and β_i characterizes the rigid-body motion of each microstructure. Traditionally, the connections between microstructures are assumed to be rigid, *i.e.*, the angle between the tangent directions of different microstructures keeps unchanged during deformation (referred to as "relative angle" for simplicity in the following). This assumption holds for lattice metamaterials under small local deformation. However, when hyperelastic lattice metamaterials undergo high stretching, the local material experiences finite deformations. Consequently, the connections are modeled as nonlinear hinges to account for the relative angular changes caused by the applied moments. This leads to

$$\begin{pmatrix} 1 & 1 & 0 & 0 \\ 0 & 1 & 1 & 0 \\ 1 & 0 & 0 & 1 \end{pmatrix} \begin{pmatrix} \beta_1 \\ \beta_2 \\ \beta_3 \\ \beta_4 \end{pmatrix} + \begin{pmatrix} 1 & -1 & 0 & 0 \\ 0 & -1 & 1 & 0 \\ 1 & 0 & 0 & -1 \end{pmatrix} \begin{pmatrix} \theta_1 \\ \theta_2 \\ \theta_3 \\ \theta_4 \end{pmatrix}, \tag{21}$$

$$= \begin{pmatrix} \pi/2 + (M_1 + M_2)/\eta \\ \pi/2 + (M_2 + M_3)/\eta \\ \pi/2 + (M_4 + M_1)/\eta \end{pmatrix}$$

where θ_i is the tangent angle at the end of each microstructure. η denotes the rotational stiffness of nonlinear hinges, which is accurately calibrated in the validation section. The deformation compatibility requires that the side lengths and interior angles of the deformed rectangle satisfy the following geometric relations:

$$\begin{pmatrix} \sin\beta_2 & \sin\beta_1 & -\sin\beta_4 & -\sin\beta_3 \\ \cos\beta_2 & -\cos\beta_1 & -\cos\beta_4 & \cos\beta_3 \end{pmatrix} \begin{pmatrix} L_1 \\ L_2 \\ L_3 \\ L_4 \end{pmatrix} = 0. \tag{22}$$

The deformed configurations of hyperelastic lattice metamaterials can be obtained by solving eqn (19)–(22) and the governing equations of the microstructures eqn (18). The longitudinal strain ε_y can be written as

$$\varepsilon_y = \frac{L_1 \sin\beta_2 + L_2 \sin\beta_1 - \sqrt{2}L}{\sqrt{2}L}. \tag{23}$$

4.2. Non-periodic boundary conditions

The mechanics of hyperelastic lattices with non-periodic boundary conditions are further explored for practical applications with boundary constraints. As depicted in Fig. 2f, the hyperelastic lattice metamaterial comprises 2 × 2 units indexed from I to IV. The connected nodes on the left boundary are pinned, while those on the right boundary are allowed to slide horizontally. Due to different boundary constraints at each end of the microstructure, the moments M_a and M_b acting on the two ends are different, resulting in non-antisymmetric deformation (Fig. 2g). The deformation of each microstructure needs to be solved individually. The connected nodes are categorized into three types: boundary nodes which have boundary constraints or loading applied; external nodes which connect two microstructures; and internal nodes which connect four microstructures (Fig. 2h). The force equilibrium in the normal and shear direction at the boundary nodes gives

$$\begin{cases} \sum\limits_{i=\mathrm{I,IV}} F_{x1}^i \sin\beta_1^i + F_{y1}^i \cos\beta_1^i + F_{x4}^i \sin\beta_4^i - F_{y4}^i \cos\beta_4^i = 2\sqrt{2}LH\sigma, \\ \sum\limits_{i=\mathrm{II,III}} F_{x3}^i \sin\beta_3^i + F_{y3}^i \cos\beta_3^i + F_{x2}^i \sin\beta_2^i - F_{y2}^i \cos\beta_2^i = -2\sqrt{2}LH\sigma, \\ \sum\limits_{i=\mathrm{I,IV}} -F_{x1}^i \cos\beta_1^i + F_{y1}^i \sin\beta_1^i + F_{x4}^i \cos\beta_4^i + F_{y4}^i \sin\beta_4^i = 0, \\ \sum\limits_{i=\mathrm{II,III}} -F_{x3}^i \cos\beta_3^i + F_{y3}^i \sin\beta_3^i + F_{x2}^i \cos\beta_2^i + F_{y2}^i \sin\beta_2^i = 0. \end{cases} \tag{24}$$

where $()_j^i$ donates the variable corresponding to the *j*th microstructure in the *i*th lattice unit. For the external and internal nodes, it requires that

$$\begin{cases} \sum F_{\mathrm{Normal}} = 0, \\ \sum F_{\mathrm{Shear}} = 0, \end{cases} \tag{25}$$

where F_{Normal} and F_{Shear} are the resultant forces in the normal and shear directions, respectively. The moment equilibrium at each connected node requires that

$$\sum M = 0. \tag{26}$$

The angle equilibrium considering the relative angular changes gives

$$\begin{pmatrix} 1 & 1 & 0 & 0 \\ 0 & 1 & 1 & 0 \\ 0 & 0 & 1 & 1 \\ 1 & 0 & 0 & 1 \end{pmatrix} \begin{pmatrix} \beta_1^i \\ \beta_2^i \\ \beta_3^i \\ \beta_4^i \end{pmatrix} + \begin{pmatrix} 1 & -1 & 0 & 0 \\ 0 & -1 & 1 & 0 \\ 0 & 0 & 1 & -1 \\ 1 & 0 & 0 & -1 \end{pmatrix} \begin{pmatrix} \theta_1^i \\ \theta_2^i \\ \theta_3^i \\ \theta_4^i \end{pmatrix} \tag{27}$$

$$= \begin{pmatrix} \pi/2 + \left(M_{1a}^i + M_{2b}^i\right)/\eta \\ \pi/2 + \left(M_{2a}^i + M_{3b}^i\right)/\eta \\ \pi/2 + \left(M_{3a}^i + M_{4b}^i\right)/\eta \\ \pi/2 + \left(M_{4a}^i + M_{1b}^i\right)/\eta \end{pmatrix}, \quad i = \mathrm{I\ to\ IV}.$$

The geometric compatibility in each lattice unit satisfies

$$\begin{pmatrix} \sin\beta_2^i & \sin\beta_1^i & -\sin\beta_4^i & -\sin\beta_3^i \\ \cos\beta_2^i & -\cos\beta_1^i & -\cos\beta_4^i & \cos\beta_3^i \end{pmatrix} \begin{pmatrix} L_1^i \\ L_2^i \\ L_3^i \\ L_4^i \end{pmatrix} = 0, \quad i = \mathrm{I\,to\,IV}. \tag{28}$$

For boundary constraints, it gives

$$\begin{cases} L_2^{\mathrm{III}}\cos\beta_2^{\mathrm{III}} + L_3^{\mathrm{II}}\cos\beta_3^{\mathrm{II}} = \sqrt{2}L, \\ L_1^{\mathrm{IV}}\cos\beta_1^{\mathrm{IV}} + L_4^{\mathrm{I}}\cos\beta_4^{\mathrm{I}} = \sqrt{2}L, \\ L_2^{\mathrm{III}}\sin\beta_2^{\mathrm{III}} - L_3^{\mathrm{II}}\sin\beta_3^{\mathrm{II}} = 0, \\ L_1^{\mathrm{IV}}\sin\beta_1^{\mathrm{I}} - L_4^{\mathrm{I}}\sin\beta_4^{\mathrm{I}} = 0. \end{cases} \tag{29}$$

The deformed configurations of hyperelastic lattice metamaterials with non-periodic boundary conditions can be obtained by solving eqn (24)–(29) and the governing equations of the microstructures.

5. Validation of the theoretical model

In this section, the developed theoretical models are validated by commercial FE simulations and experiments. Three structures are designed: hyperelastic microstructures, lattices with periodic boundary conditions and lattices with non-periodic boundary conditions.

5.1. Hyperelastic microstructures

The curvature function $R(\alpha) = \alpha^A + 1/(\alpha + B)$ $(0 \le \alpha \le \alpha_{\mathrm{end}})$ is employed to design the hyperelastic curved microstructures. Compared to the curvature function $R(\alpha) = \alpha^A$ with a single parameter A, the introduction of the term $1/(\alpha + B)$ increases the radius of curvature near the initial point, reducing the curvature jumps at antisymmetric centers of microstructures (Fig. S2, ESI†). This promotes a smooth transition and reduces the risk of stress concentration. The stretchability can be programmable by tuning the parameters A and B. For instance, by tuning the parameters A $(1 \le A \le 5)$ and B $(0.05 \le B \le 0.45)$, the ratio L_{R} of the microstructure curve length to the distance between its ends can be varied from 1.4 to 4.2 (Fig. 3a). Larger length ratios result in wider toe regions and higher stretchability of the microstructures. Three designs were constructed for validation with the following parameters: (I) A = 4.0 and B = 0.2 with L_{R} = 1.5; (II) A = 2.0 and B = 0.1 with L_{R} = 2.5; (III) A = 1.2 and B = 0.08 with L_{R} = 3.5 (Fig. 3a). All the microstructures are scaled to $L = 30\sqrt{2}$ mm. The width D = 0.6 mm and the thickness H = 2.5 mm. Each microstructure is discretized into 60 quadratic elements.

The microstructures exhibit nonlinear S-shaped stress–force curves. The deformation transfer from bending-dominated

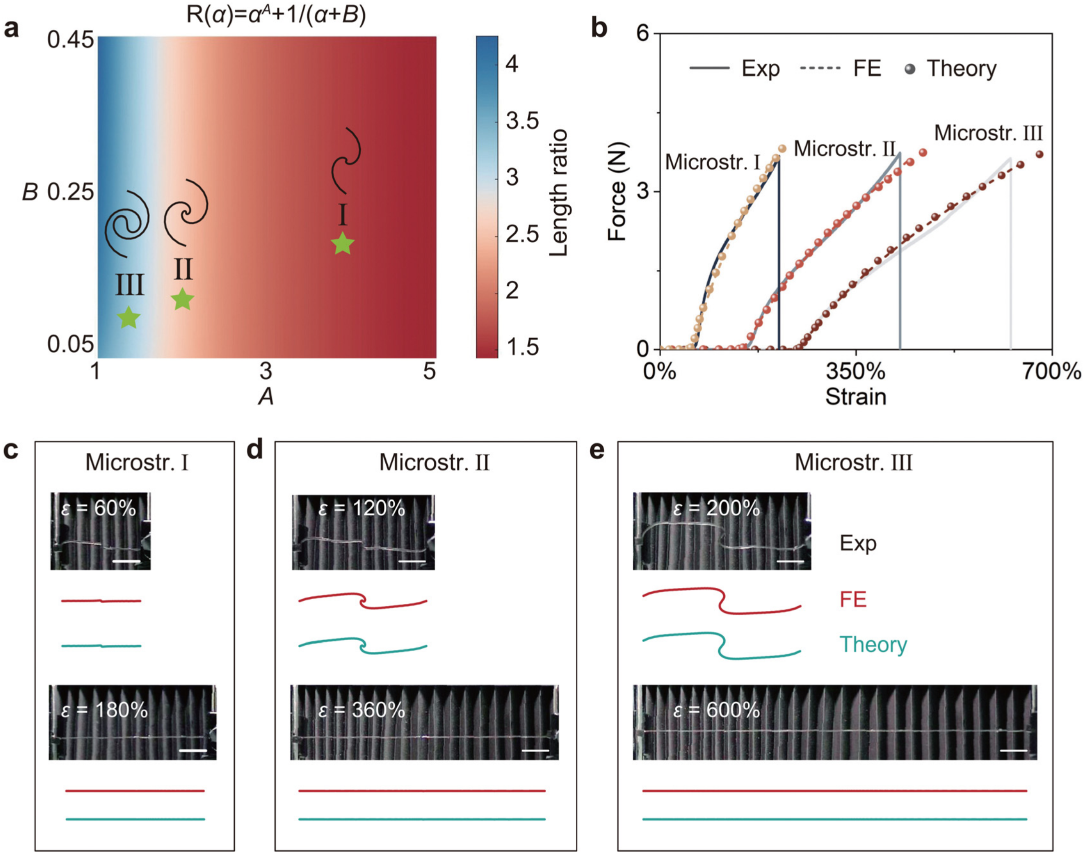

Fig. 3 Validation of the theoretical model for hyperelastic microstructures. (a) Curvature function for generating hyperelastic microstructures and the corresponding length ratio. Three microstructures are designed with varying geometric parameters. (b) Comparison of experimental, FE-simulated, and theoretical stress–strain curves for the microstructures. (c)–(e) Comparisons of experimental, FE-simulated, and theoretical deformed shapes at specific strains. All scale bars are 20 mm.

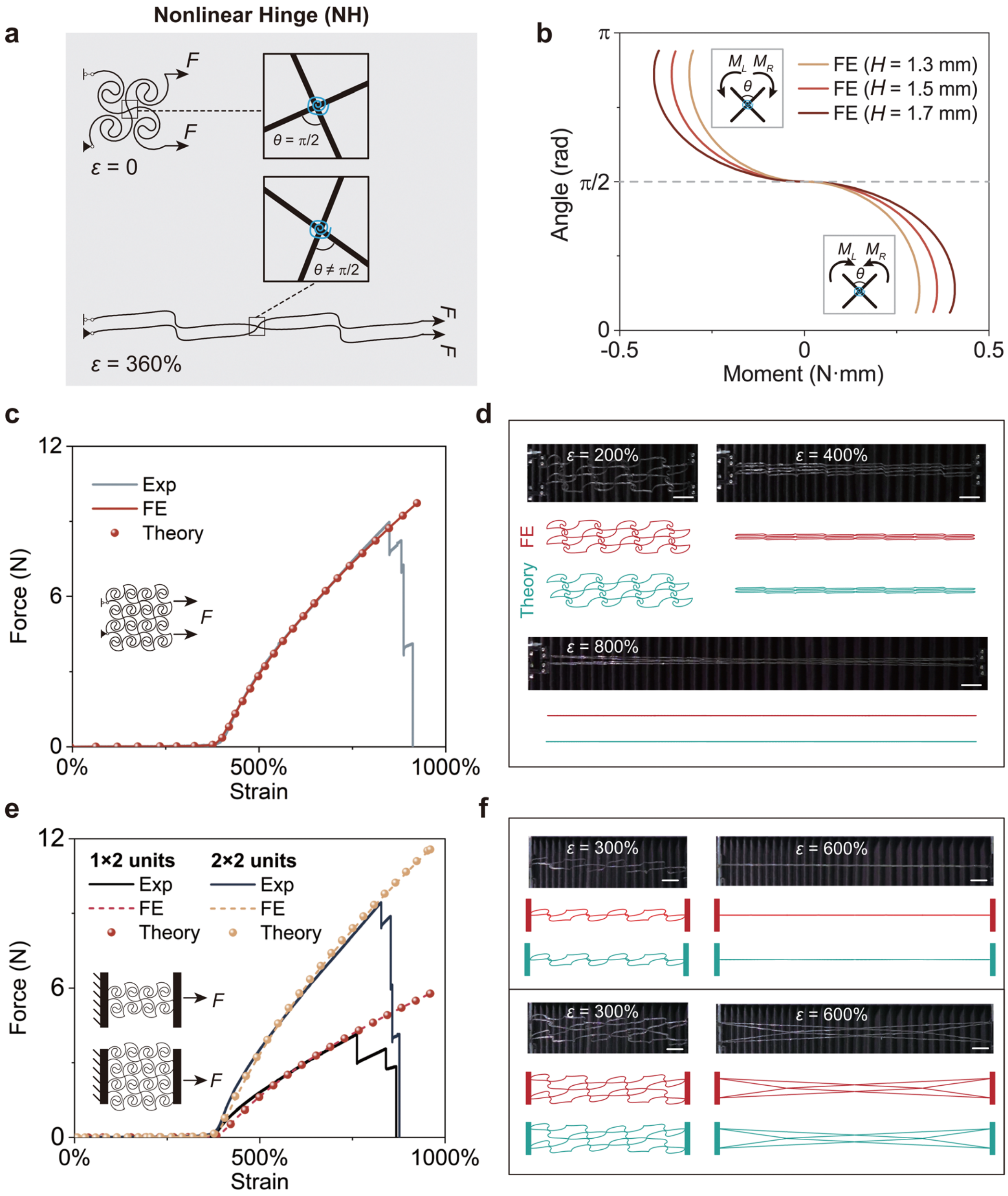

Fig. 4 Validation of the theoretical model for hyperelastic lattice metamaterials. (a) Schematic of the nonlinear hinges that indicate the angle variation between tangent lines of different microstructures under applied moments. (b) Applied moment-relative angle curves from FE-assisted calibrations. Comparison of experimental, FE simulated, and theoretical stress–strain curves for hyperelastic lattice metamaterials with (c) periodic and (d) non-periodic boundary conditions. (e) and (f) Comparison of experimental, FE simulated and theoretical deformed shapes at specific strains. All scale bars are 20 mm.

with the low modulus to stretching-dominated with the high modulus, resulted in the sequential formation of the toe and nonlinear regions. Microstructures with larger length ratio L_R show higher fracture strains. For instance, as shown in Fig. 3b, the stretchability of hyperelastic microstructures I, II, and III are 212%, 428%, and 626%, respectively, which is significantly higher than the base material (~160%). The theoretical results are in good agreement with FE simulations and experiments. The deformed shapes of the microstructures at typical strains are depicted in Fig. 3c–e. The comparison between the experimental, theoretical and FE-simulated shapes agrees well.

5.2. Lattices with periodic and non-periodic boundary conditions

To validate the theoretical model of hyperelastic lattice metamaterials with periodic boundary conditions, we first evaluate the rotational stiffness η in eqn (21). For straight beams in the linear elastic case, η is given by $12EI/L$, where EI/L is the flexural rigidity.[43] However, η is not fixed for hyperelastic lattice metamaterial due to the finite local deformation. To address this, FE-assisted calibration is performed. As depicted in Fig. 4a, the variation of relative angle due to applied moments is quantitatively characterized in ABAQUS. The FE model consists of four connected hyperelastic microstructures III (Fig. 3a), which are scaled to $L = 25\sqrt{2}/2$ mm. The bottom boundary nodes are pinned and horizontally slidable, while the upper boundary nodes are subjected to vertical forces. The applied moments are extracted from ABAQUS simulations by summing the relative moments at the connected node caused by the vertical forces. For microstructures with $D = 0.6$ mm and $H = 1.3$, 1.5, and 1.7 mm, the calculated applied moment-relative angle curves are seen to be notably nonlinear, as illustrated in Fig. 4b. When the applied moments bring the microstructures closer, the relative angle is smaller than $\pi/2$. Conversely, when the torques move the microstructures apart, the relative angle is larger than $\pi/2$. Furthermore, as the cross-sectional area increases, the variation of the relative angle decreases under the same torque. For instance, under a torque of 0.3 N mm, the relative angle for microstructures with H of 1.3, 1.5 and 1.7 mm decreases from $\pi/2$ to 0.73, 1.05 and 1.19 rad, respectively.

The strain–force curves of the hyperelastic lattice metamaterials with periodic boundary conditions are calculated by using the relationships between the applied moment and relative angle. As shown in Fig. 4c, the hyperelastic lattice metamaterial consisting of 2 × 2 units achieves a high failure strain over 850%. Similar to the hyperelastic microstructures, the hyperelastic lattice metamaterials also display an S-shaped strain–force curve, but with a wider toe region, since the geometric deformation is enabled by both the rectangular pattern and curved microstructures. The experimental, theoretical, and FE-simulated strain–force curves agree well (Fig. 4c). Comparisons of theoretically predicted, experimental, and FE-simulated deformed shapes at strains of 200%, 400%, 600%, and 800% are shown in Fig. 4d. For simplicity, a slidable setup in the boundary is used to model periodic boundary conditions.

As depicted in Fig. 4e, experiments and FE simulations are then conducted to validate the theoretical model of hyperelastic metamaterials with non-periodic boundary conditions. The hyperelastic lattice metamaterials are constructed using microstructures III with $L = 25\sqrt{2}/2$ mm, $D = 0.6$ mm and $H = 1.7$ mm. 1 × 2 units and 2 × 2 units are employed. One end of the metamaterial is fixed, and the displacement loading condition is applied to the other end. The stress–force curves also exhibit S-shapes. The failure strains are 770% for 1 × 2 units and 830% for 2 × 2 units, which are slightly smaller than those observed with periodic boundary conditions, since the non-periodic arrangements give rise to higher local stresses. The theoretically predicted stress–force curves align well with the experiments and FE simulations (Fig. 4e). The theoretical results reveal that the moments at the two ends of the microstructures with non-periodic boundary conditions are notably different. For example, $M_{3a}^{\mathrm{II}} = 0.18$ N mm and $M_{3b}^{\mathrm{II}} = 0.2$ N mm at the strain of 800% (Fig. S4, ESI†). Fig. 4f depict the deformed shapes from theory, experiment, and FE simulation at strains of 300% and 600%. The overall deformation is non-periodic, with each microstructure undergoing a distinct deformation.

6. Applications

The theoretical model can further guide multifunctional applications. The effects of material and geometric parameters of hyperelastic lattice metamaterials are investigated. Bionic hyperelastic lattices and stretchable lattice sensors are demonstrated.

6.1. Bionic hyperelastic lattices

The S-shaped stress–strain curves of hyperelastic lattice metamaterials can be tailored by tuning the microstructure geometries. A series of microstructures are designed by modifying the parameters A and B in the curvature function $R(\alpha) = \alpha^A + 1/(\alpha + B)$, as well as the width D. We utilize 2 × 2 units with non-periodic boundary conditions shown in Fig. 4e. Details of the parameters and FE-simulated results are provided in Fig. S5 (ESI†). Fig. 5a shows the stress–strain curves for microstructures designed with A values of 1.2, 2.4, 3.6, and 4.8, while $B = 0.08$ and $D = 0.6$ mm. The size of the toe region can be enlarged by increasing the length ratio L_{R}. For instance, the strains are 30%, 110%, 180% and 400% corresponding to A values of 1.2, 2.4, 3.6, and 4.8, under a relatively small stress of 0.1 kPa. Fig. 5b presents the stress–strain curves for microstructures designed with D values of 0.3, 0.6, 0.9, and 1.2 mm, while $A = 2.4$ and $B = 0.12$. The stiffness of the nonlinear region can be increased by increasing D. For instance, the stresses are 5, 12, 17 and 20 kPa corresponding to D values of 0.3, 0.6, 0.9, and 1.2 mm at a strain of 600%. These design strategies provide a method to program the S-shaped stress–strain curves (Section S7, ESI†). Developing stretchable devices that match the mechanical behaviors of biological tissues is crucial for comfortable and compliant bio-integration.[26] Numerous biological tissues exhibit large stretchability and S-shaped stress–strain curves to prevent damage from large deformations. The highly stretchable hyperelastic lattice metamaterials are promising candidates. As shown in Fig. 5c, we design the hyperelastic lattice metamaterial that mimics the S-shaped stress–strain curves of the skeletal muscle, the design parameters are $A = 1.8$, $B = 0.05$ and $D = 1.2$ mm. The experimental, FE-simulated, and theoretical results show good agreement with the natural data. Fig. 5d depicts the hyperelastic lattice metamaterial designed to replicate the S-shaped stress–strain curves of the cardiac muscle, with parameters $A = 2.2$, $B = 0.05$ and $D = 0.75$ mm.

6.2. Stretchable lattice sensors

The hyperelastic lattice metamaterials developed in this work show promise for bio-integrated device applications. Most wearable sensors do not typically experience strain exceeding 100%. However, in extreme scenarios, certain soft tissues can undergo such large deformations, in areas such as skin at joints (knee, elbow, and neck), or soft tissues under high-intensity impacts or tearing.[53–55] Sensors capable of sustaining such deformations can not only mimic the stress–strain behavior of skin at joints but also provide early warnings for potential tissue damage. Fig. 6 demonstrates the conducting hyperelastic lattice metamaterial for potential use as flexible strain sensors. As depicted in Fig. 6a, a home-made direct ink writing (DIW) 3D printer fabricates the lattice sensors using conductive silicone. Uniaxial tensile tests reveal that the material follows a Mooney–Rivlin constitutive model with $c_1 = 0.188$ MPa and $c_2 = 0.203$ MPa (Fig. S1b, ESI†). The lattice is composed of 2 × 2

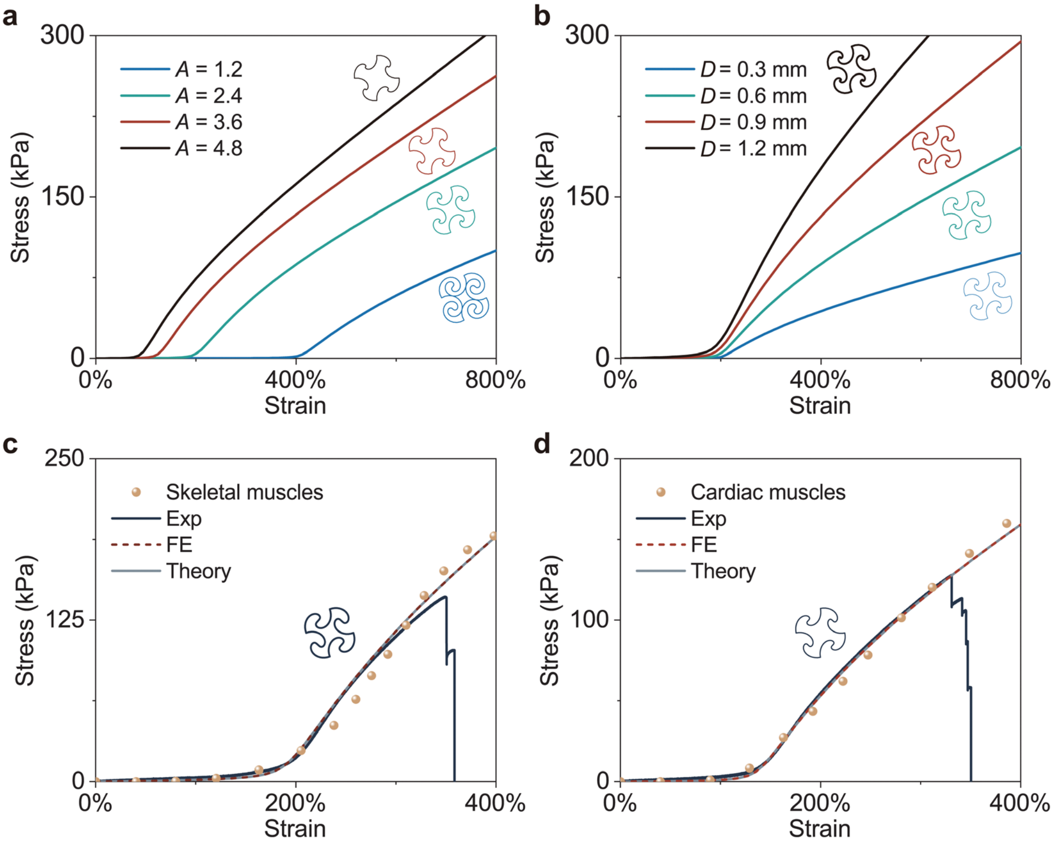

Fig. 5 Programmable mechanical behaviors. Stress–strain curves for hyperelastic microstructures designed by tuning (a) parameter *A* in curvature functions and (b) width *D*. Bionic S-shaped stress–strain curves of (c) skeletal muscle and (d) cardiac muscle. Experimental, FE-simulated, and theoretical results show good agreements. Data from ref. 18.

units with microstructures designed using parameters $A = 1.5$, $B = 0.3$, $D = 0.6$ mm, and $H = 1.5$ mm. Each microstructure functions as a stretchable resistor. When the metamaterial is subjected to uniaxial stretching, the microstructures undergo non-uniform local deformation. The resistance R_e of each element is

$$\frac{R_e}{R_0} = {\lambda_x}^2 \text{ and } R_0 = \frac{\mu l}{DH}, \tag{30}$$

where R_0 is the initial resistance and the resistivity μ is 0.04 ohm-cm. Thus, the resistance of microstructures can be obtained using

$$R_m = \sum_{e=1}^{n_e} R_e. \tag{31}$$

The equivalent circuit transformations are applied to calculate the resistance of the circuit R_c as

$$R_c = F(\{R_{mj}^i | i = 1, 2, 3, 4; j = \text{I, II, III, IV}\}), \tag{32}$$

where R_{mj}^i is the resistance of the *j*th microstructure in the *i*th lattice unit, and *F* is the relational function detailed in the ESI† (Fig. S7). The predicted conductivities from eqn (30)–(32) consistently match the measured conductivities of the lattice sensors (Fig. 6b). Fig. 6c shows the theoretically predicted and experimental deformed shapes at strains of 0%, 100%, and 200%, which are in good agreement. The color maps of theoretical local strain distributions are also shown in the panel. Two typical stages are observed: the curved microstructure bends and uncurls at the first stage, leading to a relatively small local deformation, so the resistance remains almost unchanged. In the second stage, the microstructure is nearly straightened, and tension dominates the deformation, causing a sharp increase in local deformation and resistance.

The resistance of the lattice sensor was measured under different temperature and humidity conditions (Fig. S6, ESI†), with the environment controlled using a heater and humidifier. Tests were conducted over a temperature range of 10 to 70 °C and a humidity range of 30% to 75%. As shown in Fig. 6d, the resistance of the undeformed lattice conductors increases with temperature. For example, at 40% humidity, the resistance increased from 16.4 Ω at 10 °C to 18.3 Ω at 70 °C. Conversely, humidity has a smaller effect on resistance (Fig. 6e). At 20 °C, the resistance increased from 16.4 Ω at 30% humidity to 16.8 Ω at 75% humidity (Fig. 6e).

Stretchable lattice sensors are then demonstrated to monitor heartbeats *in vitro*. A cyclically deforming balloon was used to mimic a beating heart, encapsulated by a lattice conductor, and the conductivity was measured at both ends (Fig. 6d). As the balloon deforms, the lattice metamaterial with low stiffness

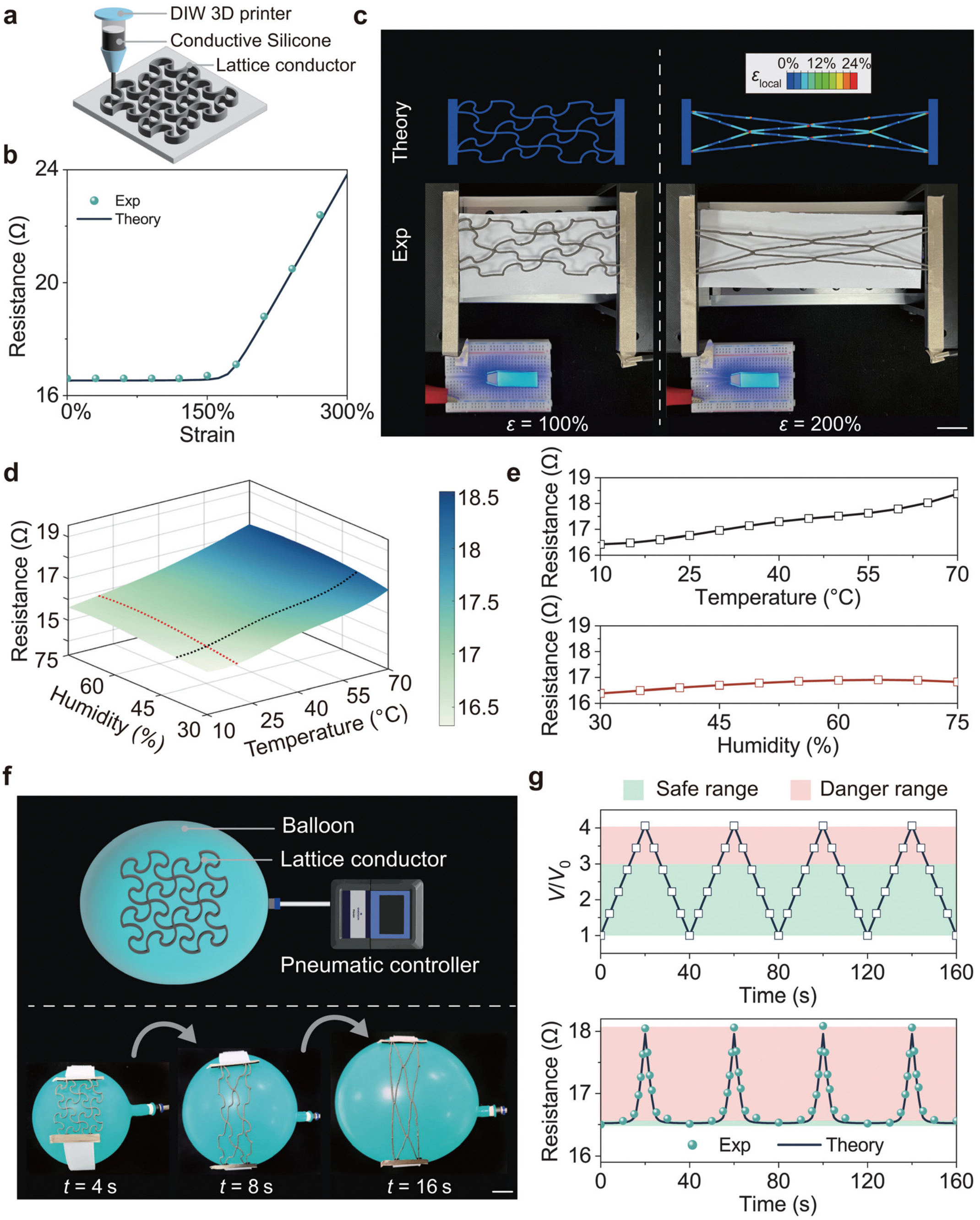

Fig. 6 Stretchable lattice sensors. (a) Fabrication of lattice sensors using a custom DIW 3D printer with conductive silicone, where each microstructure acts as a stretchable resistor. (b) Comparison of experimental and theoretical strain–resistance curves. (c) Theoretical and experimental deformed shapes at specific strains. (d) The relationship between the resistance of lattice conductors and both temperature and humidity. (e) The resistance variation with temperature at 40% humidity and with humidity at 20 °C. (f) Encapsulation of a cyclically deforming balloon within a lattice conductor. (g) Cyclic volume changes of the balloon and corresponding theoretical and experimental resistances of the lattice conductor. All scale bars are 20 mm.

and high deformability can conformally deform around the balloon surface. As shown in Fig. 6e, a pneumatic controller regulates the air input to achieve cyclical volume changes. We define $1 \leq V/V_0 \leq 3$ as the safe range for normal heartbeats and $V/V_0 > 3$ as the danger zone for abnormal heartbeats. The theoretically calculated resistances match the experimental results. In the safe range, resistance changes are relatively small, whereas in the danger zone, resistance sharply increases with volume. These stretchable lattice sensors can also be used for human motion capture and health monitoring.

6.3. Remote controls using lattice sensors

Hyperelastic lattice metamaterials are designed to control an industrial robot (Fig. 7). The sensor consists of 3 × 1 units, encapsulated using acrylic VHB. It is worn on the finger joint, which can adapt to large strain during flexion. The geometric and material parameters

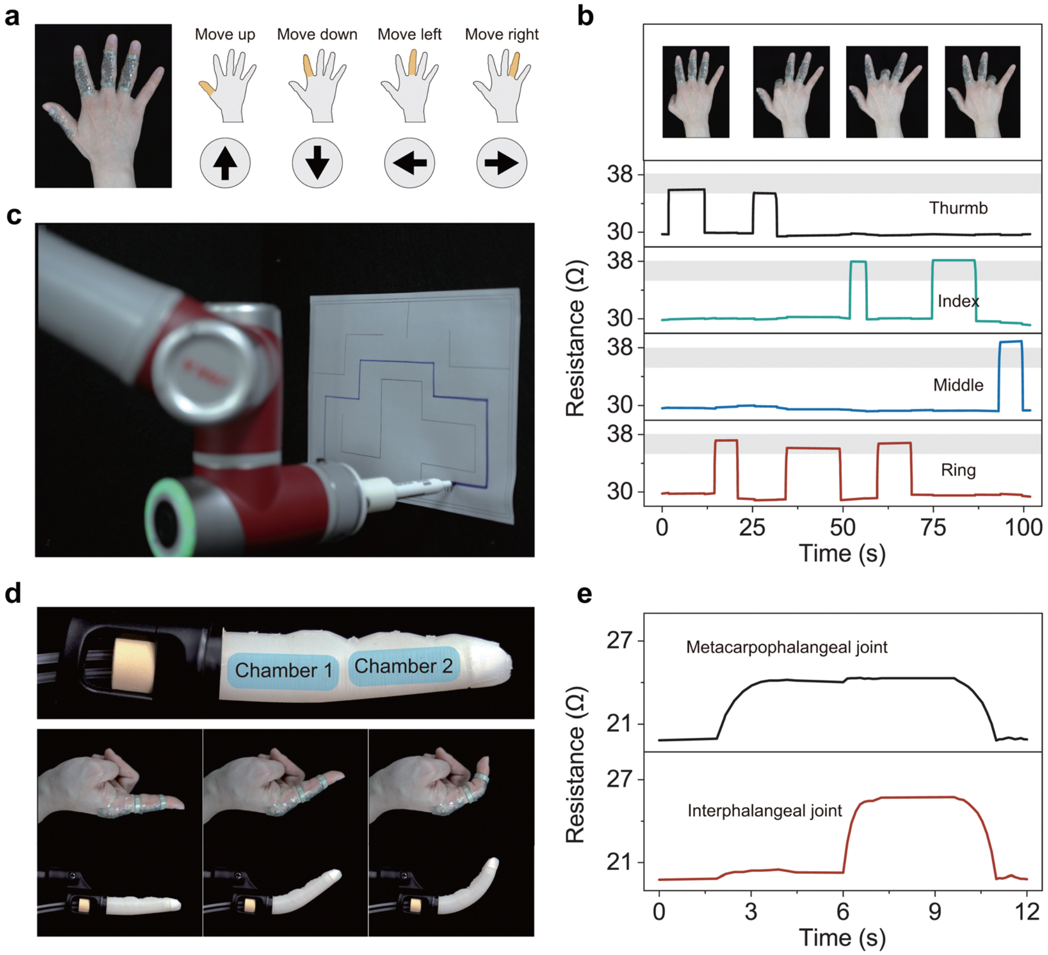

Fig. 7 Remote controls of an industrial robot and soft robotic finger using metamaterial sensors. (a) Metamaterial sensor monitoring finger bending and controlling the robot's movement in specific directions. (b) Relative resistance changes in four channels during the maze exploration task. (c) Robot movement along predefined trajectories based on sensor input. (d) Metamaterial sensor monitoring multi-joint finger motion to control a soft robotic finger. (e) Relative resistance changes at the metacarpophalangeal and interphalangeal joints during finger motion.

of the microstructures are the same as in Fig. 6a, with the height modified to 1 mm. The resistance of the hyperelastic lattice metamaterials is measured using a multi-channel resistance acquisition system (Anbai, AT5130) to continuously track finger movements. Each finger movement is pre-programmed to control a specific direction of the robots movement (Fig. 7a), allowing the operator to navigate a maze remotely (Fig. 7b and c and Movie S1, ESI†).

Another metamaterial sensor is designed to control a soft robotic finger. The lattice (composed of 2 × 1 units) is placed at the metacarpophalangeal and interphalangeal joints to monitor multi-joint bending (Fig. 7d). The resistance signals of the lattices are used to continuously control the inflation of two pneumatic chambers (Fig. 7e). The results show that the soft finger can replicate the motions of the human finger in real time (Movie S2, ESI†). These demonstrations highlight the ability of our metamaterial sensors to accommodate large deformations at joint areas.

7. Discussion and conclusion

The significance of our work lies in three key aspects: (1) we achieve S-shaped stress–strain curves using hyperelastic lattice metamaterials, which combines hyperelastic materials and lattice structures with curved microstructures. (2) We develop a theoretical model that accurately predicts and inversely designs the S-shaped stress–strain curves, considering the hierarchical structures and material nonlinearity. (3) We demonstrate highly stretchable lattice sensors that mimic S-shaped stress–strain curves using the theoretical framework.

Previous studies on lattice metamaterials have mainly focused on structures exhibiting J-shaped stress–strain curves, typically assuming linear elastic behavior. Recently, several theoretical models have explored hyperelastic lattice with straight microstructures, utilizing the principle of stationary potential energy.[38,56] But the hyperelastic behaviors of curved lattices have not been investigated theoretically. Additionally, periodic boundary conditions were often assumed. In this work, the theoretical model considers material hyperelasticity, curved microstructures and both periodic and non-periodic boundary conditions. A detailed comparison of our theoretical model with existing studies is provided in Table S1 (ESI†).

Sensors that replicate bionic stress–strain curves are essential for integration with organisms, as they minimize the damage induced by the mechanical mismatch. However, designs based on experimental experience often fail to replicate the nonlinear stress–strain responses of biological tissues. Developing theoretical models can not only offer insights into the underlying physics but also provide efficient inverse design and optimization of stress–strain sensors. In this work, the theoretical model enables the design of soft sensors with bionic S-shaped stress–strain behaviors, high stretchability ($>300\%$) and predictable resistant changes under load. Previous research has rarely achieved all three of these key performance metrics. A comparative analysis of three key sensor performance metrics is presented in Table S2 (ESI†).

In summary, we propose an integrated theoretical, FE simulation and experimental design framework for 3D printed hyperelastic lattice metamaterials with curved microstructures. In the developed hierarchical theoretical model, the microstructures are modeled by extending a Timoshenko-type beam formulation that accounts for curved geometries and hyperelastic material. The model is then combined with the analysis of equilibrium and deformation compatibility which consider non-rigid connections between microstructures to elucidate the deformation mechanisms of hyperelastic lattice metamaterials. Both periodic and nonperiodic boundary conditions are addressed. The theoretical results show that hyperelastic lattice metamaterials exhibit S-shaped stress–strain curves consisting of toe and nonlinear regions. Experiments and commercial FE simulations are conducted to validate the theoretical models. The framework can enable customizable mechanical behaviors by tuning the geometric and material parameters. The designed hyperelastic lattice metamaterials achieve high stretchability (over 800%) and exhibit stress–strain curves mimicking biological tissues. We demonstrate the highly stretchable lattice sensors with predictable electrical properties for remote controls. This work provides systematic guidelines for designing and manufacturing hyperelastic lattice metamaterials, paving the way for robots with realistic human mechanosensation.

Data availability

The data supporting this article have been included as part of the ESI.†

Conflicts of interest

The authors declare that they have no known competing financial interests or personal relationships that could have appeared to influence the work reported in this paper.

Acknowledgements

D. W. acknowledges support from the National Natural Science Foundation of China (Grant No. 52275025), the National Key Research and Development Program of China (No. 2022YFB4700900), and the State Key Laboratory of Mechanical System and Vibration (Grant No. MSVZD202401).

References

1 Z. Liu, X. Hu, R. Bo, Y. Yang, X. Cheng, W. Pang, Q. Liu, Y. Wang, S. Wang and S. Xu, *et al.*, A three-dimensionally architected electronic skin mimicking human mechanosensation, *Science*, 2024, **384**(6699), 987–994.

2 S. H. Kim, A. Basir, R. Avila, J. Lim, S. W. Hong, G. Choe, J. H. Shin, J. H. Hwang, S. Y. Park and J. Joo, *et al.*, Strain-invariant stretchable radio-frequency electronics, *Nature*, 2024, **629**(8014), 1047–1054.

3 C. Zhao, J. Park, S. E. Root and Z. Bao, Skin-inspired soft bioelectronic materials, devices and systems, *Nat. Rev. Bioeng.*, 2024, **2**(8), 671–690.

4 S. Jin, H. Choi, D. Seong, C.-L. You, J.-S. Kang, S. Rho, W. B. Lee, D. Son and M. Shin, Injectable tissue prosthesis for instantaneous closed-loop rehabilitation, *Nature*, 2023, **623**(7985), 58–65.

5 H. Yuk, C. E. Varela, C. S. Nabzdyk, X. Mao, R. F. Padera, E. T. Roche and X. Zhao, Dry double-sided tape for adhesion of wet tissues and devices, *Nature*, 2019, **575**(7781), 169–174.

6 M. Vatankhah-Varnosfaderani, W. F. Daniel, M. H. Everhart, A. A. Pandya, H. Liang, K. Matyjaszewski, A. V. Dobrynin and S. S. Sheiko, Mimicking biological stress-strain behaviour with synthetic elastomers, *Nature*, 2017, **549**(7673), 497–501.

7 X. Cheng, Z. Fan, S. Yao, T. Jin, Z. Lv, Y. Lan, R. Bo, Y. Chen, F. Zhang and Z. Shen, *et al.*, Programming 3d curved mesosurfaces using microlattice designs, *Science*, 2023, **379**(6638), 1225–1232.

8 A. Rafsanjani, K. Bertoldi and A. R. Studart, Programming soft robots with flexible mechanical metamaterials, *Sci. Rob.*, 2019, **4**(29), eaav7874.

9 D. Rus and M. T. Tolley, Design, fabrication and control of soft robots, *Nature*, 2015, **521**(7553), 467–475.

10 D. Stuart-Fox, L. Ng, M. A. Elgar, K. Hölttä-Otto, G. E. Schröder-Turk, N. H. Voelcker and G. S. Watson, Bio-informed materials: three guiding principles for innovation informed by biology, *Nat. Rev. Mater.*, 2023, **8**(9), 565–567.

11 M. A. Meyers, J. McKittrick and P.-Y. Chen, Structural biological materials: critical mechanics-materials connections, *Science*, 2013, **339**(6121), 773–779.

12 A. Pissarenko and M. A. Meyers, The materials science of skin: Analysis, characterization, and modeling, *Prog. Mater. Sci.*, 2020, **110**, 100634.

13 Y. J. No, M. Castilho, Y. Ramaswamy and H. Zreiqat, Role of biomaterials and controlled architecture on tendon/ligament repair and regeneration, *Adv. Mater.*, 2020, **32**(18), 1904511.

14 G. A. Holzapfel, T. C. Gasser and R. W. Ogden, A new constitutive framework for arterial wall mechanics and a comparative study of material models, *J. Elasticity Phys. Sci. Solids*, 2000, **61**, 1–48.

15 G. C. Engelmayr Jr, M. Cheng, C. J. Bettinger, J. T. Borenstein, R. Langer and L. E. Freed, Accordion-like honeycombs for tissue engineering of cardiac anisotropy, *Nat. Mater.*, 2008, **7**(12), 1003–1010.

16 Y.-L. Sun, Z.-P. Luo, A. Fertala and K.-N. An, Direct quantification of the flexibility of type i collagen monomer, *Biochem. Biophys. Res. Commun.*, 2002, **295**(2), 382–386.

17 P. Fratzl, *Collagen: structure and mechanics, an introduction*, Springer, 2008, pp. 1–13.

18 H. L. Granzier and T. C. Irving, Passive tension in cardiac muscle: contribution of collagen, titin, microtubules, and intermediate filaments, *Biophys. J.*, 1995, **68**(3), 1027–1044.

19 Y.-C. Fung, *Biomechanics: mechanical properties of living tissues*, Springer Science & Business Media, 2013.

20 R. Chaudhary, P. Fabbri, E. Leoni, F. Mazzanti, R. Akbari and C. Antonini, Additive manufacturing by digital light processing: a review, *Prog. Addit. Manuf.*, 2023, **8**(2), 331–351.

21 S.-M. Chang, S. Hur, J. Park, D.-G. Lee, J. Shin, H. S. Kim, S. E. Song, J. M. Baik, M. Kim and H.-C. Song, *et al.*, Optimization of piezoelectric polymer composites and 3d printing parameters for flexible tactile sensors, *Addit. Manuf.*, 2023, **67**, 103470.

22 T. J. Buchner, S. Rogler, S. Weirich, Y. Armati, B. G. Cangan, J. Ramos, S. T. Twiddy, D. M. Marini, A. Weber and D. Chen, *et al.*, Vision-controlled jetting for composite systems and robots, *Nature*, 2023, **623**(7987), 522–530.

23 J. Liu, D. Yan, W. Pang and Y. Zhang, Design, fabrication and applications of soft network materials, *Mater. Today*, 2021, **49**, 324–350.

24 P. Jiao, J. Mueller, J. R. Raney, X. Zheng and A. H. Alavi, Mechanical metamaterials and beyond, *Nat. Commun.*, 2023, **14**(1), 6004.

25 A. Du Plessis, C. Broeckhoven, I. Yadroitsava, I. Yadroitsev, C. H. Hands, R. Kunju and D. Bhate, Beautiful and functional: a review of biomimetic design in additive manufacturing, *Addit. Manuf.*, 2019, **27**, 408–427.

26 J. Park, S. Choi, A. H. Janardhan, S.-Y. Lee, S. Raut, J. Soares, K. Shin, S. Yang, C. Lee and K.-W. Kang, Electromechanical cardioplasty using a wrapped elasto-conductive epicardial mesh, *Sci. Transl. Med.*, 2016, **8**(344), 344ra86.

27 H. Song, G. Luo, Z. Ji, R. Bo, Z. Xue, D. Yan, F. Zhang, K. Bai, J. Liu and X. Cheng, Highly-integrated, miniaturized, stretchable electronic systems based on stacked multilayer network materials, *Sci. Adv.*, 2022, **8**(11), eabm3785.

28 S. Oh, T. Song, M. Mahato, J. Kim, H. Yoo, M. Lee, M. Khan, W. Yeo and I. Oh, Easy-to-wear auxetic sma knot-architecture for spatiotemporal and multimodal haptic feedbacks, *Adv. Mater.*, 2023, **35**(47), 2304442.

29 K.-I. Jang, H. U. Chung, S. Xu, C. H. Lee, H. Luan, J. Jeong, H. Cheng, G.-T. Kim, S. Y. Han and J. W. Lee, Soft network composite materials with deterministic and bio-inspired designs, *Nat. Commun.*, 2015, **6**(1), 6566.

30 X. Xin, L. Liu, Y. Liu and J. Leng, 4d printing auxetic metamaterials with tunable, programmable, and reconfigurable mechanical properties, *Adv. Funct. Mater.*, 2020, **30**(43), 2004226.

31 S. Cao, Y. Wei, R. Bo, X. Yun, S. Xu, Y. Guan, J. Zhao, Y. Lan, B. Zhang and Y. Xiong, Inversely engineered biomimetic flexible network scaffolds for soft tissue regeneration, *Sci. Adv.*, 2023, **9**(39), eadi8606.

32 Y. Ma, X. Feng, J. A. Rogers, Y. Huang and Y. Zhang, Design and application of 'j-shaped' stress-strain behavior in stretchable electronics: a review, *Lab Chip*, 2017, **17**(10), 1689–1704.

33 S. Cao, J. Wu, Y. Lai, Z. Shen, J. Liu, R. Bo, J. Chang, Z. Wang and Y. Zhang, A phenomenological framework for modeling of nonlinear mechanical responses in soft network materials with arbitrarily curved microstructures, *Extreme Mech. Lett.*, 2022, **55**, 101795.

34 Q. Ma, H. Cheng, K.-I. Jang, H. Luan, K.-C. Hwang, J. A. Rogers, Y. Huang and Y. Zhang, A nonlinear mechanics model of bio-inspired hierarchical lattice materials consisting of horseshoe microstructures, *J. Mech. Phys. Solids*, 2016, **90**, 179–202.

35 Q. Ma and Y. Zhang, Mechanics of fractal-inspired horseshoe microstructures for applications in stretchable electronics, *J. Appl. Mech.*, 2016, **83**(11), 111008.

36 J. Liu, D. Yan and Y. Zhang, Mechanics of unusual soft network materials with rotatable structural nodes, *J. Mech. Phys. Solids*, 2021, **146**, 104210.

37 L. Dong, J. Wang and D. Wang, Modeling and design of three-dimensional voxel printed lattice metamaterials, *Addit. Manuf.*, 2023, **69**, 103532.

38 Y. Zhang, K. Yu, K. H. Lee, K. Li, H. Du and Q. Wang, Mechanics of stretchy elastomer lattices, *J. Mech. Phys. Solids*, 2022, **159**, 104782.

39 H. Chen, F. Zhu, K.-I. Jang, X. Feng, J. A. Rogers, Y. Zhang, Y. Huang and Y. Ma, The equivalent medium of cellular substrate under large stretching, with applications to stretchable electronics, *J. Mech. Phys. Solids*, 2018, **120**, 199–207.

40 S. Han, M. K. Kim, B. Wang, D. S. Wie, S. Wang and C. H. Lee, Mechanically reinforced skin-electronics with networked nanocomposite elastomer, *Adv. Mater.*, 2016, **28**(46), 10257–10265.

41 J. Liu and Y. Zhang, A mechanics model of soft network materials with periodic lattices of arbitrarily shaped filamentary microstructures for tunable Poisson's ratios, *J. Appl. Mech.*, 2018, **85**(5), 051003.

42 B. Sadri, D. Goswami, M. Sala de Medeiros, A. Pal, B. Castro, S. Kuang and R. V. Martinez, Wearable and implantable epidermal paper-based electronics, *ACS Appl. Mater. Interfaces*, 2018, **10**(37), 31061–31068.

43 Y. Yin, Z. Zhao and Y. Li, Theoretical and experimental research on anisotropic and nonlinear mechanics of periodic network materials, *J. Mech. Phys. Solids*, 2021, **152**, 104458.

44 Y. Chen, T. Li, F. Scarpa and L. Wang, Lattice metamaterials with mechanically tunable poissons ratio for vibration control, *Phys. Rev. Appl.*, 2017, **7**(2), 024012.

45 B. K. Ashley, M. S. Brown, Y. Park, S. Kuan and A. Koh, Skin-inspired, open mesh electrochemical sensors for lactate and oxygen monitoring, *Biosens. Bioelectron.*, 2019, **132**, 343–351.

46 R. Lima, P. Martins, N. Ramião and R. Jorge, Methodology for mechanical characterization of soft biological tissues: arteries, *Procedia Eng.*, 2015, **110**, 74–81.

47 X. Yan, Q. Chen, L. Zhu, H. Chen, D. Wei, F. Chen, Z. Tang, J. Yang and J. Zheng, High strength and self-healable gelatin/polyacrylamide double network hydrogels, *J. Mater. Chem. B*, 2017, **5**(37), 7683–7691.

48 H. Haider, C. H. Yang, W. J. Zheng, J. H. Yang, M. X. Wang, S. Yang, M. Zrínyi, Y. Osada, Z. Suo and Q. Zhang,

Exceptionally tough and notch-insensitive magnetic hydrogels, *Soft Matter*, 2015, **11**(42), 8253–8261.

49 Z. Zhang, J. Luo, S. Zhao, S. Ge, J.-M. Y. Carrillo, J. K. Keum, C. Do, S. Cheng, Y. Wang and A. P. Sokolov, Surpassing the stiffness-extensibility trade-off of elastomers via mastering the hydrogen-bonding clusters, *Matter*, 2022, **5**(1), 237–252.

50 P. Wriggers, *Nonlinear finite element methods*, Springer Science & Business Media, 2008.

51 C. Perez-Garcia, J. Aranda-Ruiz, R. Zaera and D. Garcia-Gonzalez, Beam formulation and fe framework for architected structures under finite deformations, *Eur. J. Mech. A/Solids*, 2022, **96**, 104706.

52 E. Reissner, On one-dimensional finite-strain beam theory: the plane problem, *Z. Angew. Math. Phys.*, 1972, **23**(5), 795–804.

53 W. Yang, V. R. Sherman, B. Gludovatz, E. Schaible, P. Stewart, R. O. Ritchie and M. A. Meyers, On the tear resistance of skin, *Nat. Commun.*, 2015, **6**(1), 6649.

54 R. L. Gajdosik, Passive extensibility of skeletal muscle: review of the literature with clinical implications, *Clin. Biomech.*, 2001, **16**(2), 87–101.

55 H. L. Granzier and T. C. Irving, Passive tension in cardiac muscle: contribution of collagen, titin, microtubules, and intermediate filaments, *Biophys. J.*, 1995, **68**(3), 1027–1044.

56 T. Li, Y. Jiang, K. Yu and Q. Wang, Stretchable 3d lattice conductors, *Soft Matter*, 2017, **13**(42), 7731–7739.